

# 1 Speckle-free self-supervised learning for imaging 2 through unknown random diffusers with 3 unknown plane displacements and rotations

4 ZICHENG HUANG<sup>1</sup>, MENGYANG SHI<sup>1</sup>, JIAHUI MA<sup>1</sup>, ZHISHUN GUO<sup>1</sup>,  
5 YESHENG GAO<sup>1,\*</sup> AND XINGZHAO LIU<sup>1</sup>

6 *<sup>1</sup>State Key Laboratory of Advanced Optical Communication Systems and Networks, Shanghai Jiao Tong  
7 University, 800 Dongchuan Road, Shanghai 200240, China*

8 \*ysgao@sjtu.edu.cn

9 **Abstract:** Recently, deep learning (DL) methods have been extensively developed for imaging  
10 through scattering media. However, most learning methods rely on training with pairs of  
11 target-speckle data and lack integration with the physical imaging process. Here, we report  
12 a speckle-free self-supervised learning method that could be applied for imaging through  
13 unknown random diffusers with unknown plane displacements and rotations. Unlike traditional  
14 learning-based methods, our approach optimizes speckle reconstruction by leveraging the physical  
15 process of scattering imaging instead of fitting to "speckle-label" pairs. Our method models  
16 the scattered light field across potential scattering conditions to generate speckle patterns and  
17 extracts their correlation properties for model training and optimization. This eliminates the need  
18 for any pre-collected speckle patterns during network training. Our speckle-free method exhibits  
19 high reconstruction performance for imaging in unseen scattering conditions. We validate  
20 its performance across 440 scattering conditions, including plane displacements, rotations,  
21 and combinations. Our method outperforms physics-informed learning approaches regarding  
22 reconstruction performance, consistency, and generalization ability in scalable imaging scenarios.  
23 This approach addresses the challenges of model generalization and extensive data collection for  
24 training, demonstrating its feasibility and superiority for imaging through unknown scattering  
25 media in novel scenarios.

## 26 1. Introduction

27 Imaging through scattering media has been a pervasive challenging issue in many fields, varying  
28 from microscope imaging through biological issues to macroscopic astronomical observations  
29 and remote sensing [1–4]. In past decades, many methods based on ballistic light measurement,  
30 wavefront shaping, transmission matrix, point spread function, and speckle correlation were  
31 developed to settle this challenge [5–14]. In recent years, learning-based methods such as support  
32 vector machines, machine learning, and deep learning have shown strong reconstruction capability  
33 in imaging through scattering media without building an explicit model [15–18]. However,  
34 as a data-driven method, the reconstruction performance of the learning-based method highly  
35 relies on the training data, i.e., labeled speckle patterns [19]. Besides, imaging generalization  
36 capability for unknown scattering conditions such as different scattering media and different  
37 imaging distances is essential in speckle reconstruction [20, 21]. Hence, the collection and  
38 training costs of massive-scale speckle patterns become challenging issues in imaging through  
39 scattering media.

40 Deep learning (DL) proved to be an effective and superior method in computing imaging due to  
41 its powerful feature extraction ability [22, 23]. The DL-based methods investigate the properties  
42 of the scattering media and provide high-performance speckle reconstruction solutions [24–27].  
43 Li et al., for the first time, introduced the U-type structure convolutional neural network "IDiffNet"  
44 in speckle reconstruction [28]. Y.Li. et al. developed an Unet for imaging through scalable  
45 diffusers [29]. Sun et al. proposed a generative adversarial network (GAN) with a speckle

46 classification front network for imaging through dynamic scattering media [30]. Wang et al.  
47 introduced the self-attention mechanism to strengthen the model feature extraction capability  
48 and achieved a range of 75 times that of the memory effect (ME) range for sparse pattern  
49 reconstruction. [31] However, the DL-based methods were modeled to characterize the inverse  
50 scattering process and need speckle patterns in different scattering conditions to enhance model  
51 generalization capability.

52 Physics-informed learning methods provide scalable imaging through unknown scattering  
53 media without massive speckle data training [32]. Zhu et al. developed physical-aware learning  
54 that combines the speckle correlation patterns to extend the imaging depth-of-field for imaging  
55 through unknown scattering media [33]. Hu et al. developed a model-free semi-supervised  
56 learning method with adaptive inverse mapping for imaging through dynamic scattering media [34].  
57 Shi et al. proposed an unsupervised learning method that only needs one frame speckle pattern and  
58 unpaired targets to optimize the network based on speckle correlation physics information [35].  
59 Hence, the physical information of the scattering process is essential to reduce model data reliance  
60 and enhance generalization capability.

61 In this work, we propose a speckle-free self-supervised learning method for imaging through  
62 unknown scattering media with unknown displacements and rotations of the scattering media  
63 plane. The overall training process of the proposed method does not need to collect any speckle  
64 patterns to optimize the model. The method only needs some basic imaging parameters and  
65 imaging targets to generate speckle patterns in potential scattering scenarios. Unlike the DL-based  
66 methods simply mapping the speckle patterns to targets, the proposed method is designed based  
67 on the physical process and introduce the auto-correlation information to the model. The  
68 speckle-free method demonstrates high speckle reconstruction performance in unseen scattering  
69 conditions. We validate the reconstruction performance in 440 practical scattering imaging  
70 conditions. The speckle-free methods outperform comparative state-of-the-art methods with  
71 superior imaging performance, remarkable consistency, and strong generalization capabilities.  
72 Our method addresses the training reliance on speckle data and provides more possibility for  
73 imaging in scalable scattering scenarios.

## 74 2. Methods

### 75 2.1. Scattering imaging model

76 In imaging through scattering media, the optical memory effect (OME) is discovered in several  
77 existing scattering scenarios [36–38]. According to the OME theory, the optical imaging system  
78 could be modeled as a linear system in the range of OME. Here, we model The scattered light  
79 field for imaging through scattering media as the convolution of the target and the point spread  
80 function (PSF) of the optical imaging system:

$$I = O * S, \quad (1)$$

81 Where the  $(*)$  represents the convolution operation; the  $O$  represents the intensity information of  
82 the incident light target; the  $I$  represents the speckle pattern information of the scattered light;  
83 the  $S$  represents the PSF of the optical scattering imaging system.

84 Here, we mainly consider the strongly scattering media, i.e., ground glass diffuser as the  
85 random media. Here, we model the light-scattering process as three individual processes: the  
86 incident light carried target information arrives at the diffuser plane, the light passes through the  
87 random diffuser, and the scattered light arrives at the detection plane. As Fig.1 (a) depicts, we  
88 utilize the Fresnel propagation to model the light propagation in free space. The random diffuser  
89 is assumed to be thin and non-absorbing. Hence, the scattered light field could be expressed as  
90 follows:

$$I(x, y) = ((O(x, y) * h(x, y)) \cdot T(x, y)) * h(x, y), \quad (2)$$

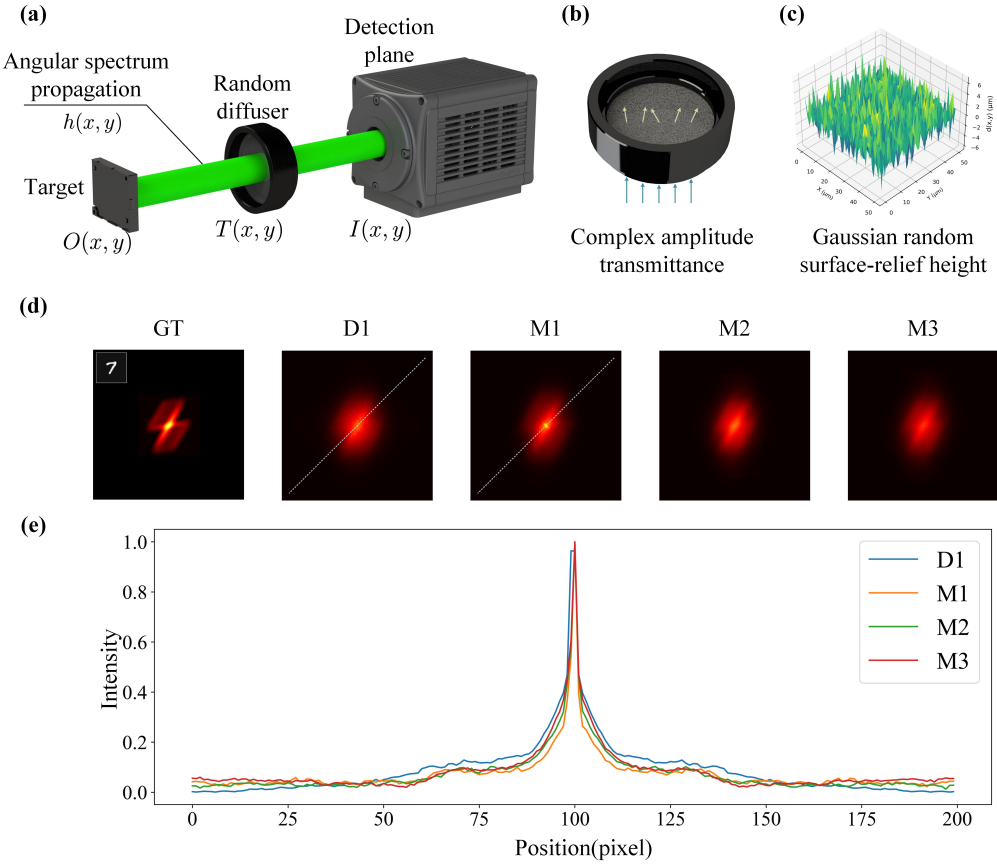


Fig. 1. (a). Scattering imaging model. (b). Complex amplitude transmittance of the proposed model. (c). Gaussian random surface-relief height of the proposed model. (d). Speckle correlation of one target produced by practical diffuser D1 (220-grit) and scattering imaging models M1 (120-grit), M2 (220-grit), and M3 (600-grit). (e). Intensity values of the white dash line in the autocorrelation.

Where the  $O(x, y)$  and  $I(x, y)$  represent the incident light field and scattered light field of the optical imaging system; the  $h(x, y)$  represents the angular spectrum propagation transfer function, which could be regarded as a linear spatial frequency domain filter with propagation distance  $d$ :

$$H(f_X, f_Y) = \exp \left[ j \frac{2\pi d}{\lambda} \sqrt{1 - (\lambda f_X)^2 - (\lambda f_Y)^2} \right], \quad (3)$$

Where the  $H(f_X, f_Y)$  represents the frequency spectrum function of the angular spectrum propagation transfer function  $h(x, y)$ ; the  $d$  represents the light propagation in free space; the  $\lambda$  represents the light wavelength; the  $f_X$  and  $f_Y$  represent the spatial frequency spectrum coordinates.

Here, we utilize the complex phase and amplitude modulation to model the random diffuser's influence on the incident light. We visualize the complex amplitude transmittance of the random diffuser in Fig.1 (b), the  $T(x, y)$  in Eq.(2) represents the complex amplitude transmittance of the random diffuser, which could be expressed as follows:

$$T(x, y) = \exp[j\varphi(x, y)], \quad (4)$$

102 According to the Ref. [39], the phase  $\varphi(x, y)$  is related to the random diffuser surface-relief  
 103 height  $h(x, y)$  and the material refractive index  $n_d(x, y)$ . Hence, the random phase distribution  
 104  $\varphi(x, y)$  could be expressed as follows:

$$\varphi(x, y) = \frac{2\pi}{\lambda} [n_d(x, y) - 1] d(x, y), \quad (5)$$

105 The  $n_d(x, y)$  is a constant value that is related to the diffuser material, which is modeled as  
 106 approximately 1.52 in Eq.(5). Hence, the random phase distribution  $\varphi(x, y)$  is determined by  
 107 the random surface-relief height  $d(x, y)$ . In diffuser-producing craft, different sizes of particles  
 108 are used to grind the glass, producing random diffusers with different grit numbers. Hence, the  
 109 size of particles determines the surface-relief height. Here, we model the random surface-relief  
 110 height  $d(x, y)$  as the random Gaussian distribution function of the diffuser grit number  $G$  and the  
 111 discrete sample locations  $(x, y)$ :

$$d(x, y) \sim \mathcal{N}(\mu_d, \sigma_d^2), \quad (6)$$

112 Where the  $\mu_d$  and  $\sigma_d$  represent the mean value and variance of the surface-relief height, which are  
 113 set as  $\mu_d = 0.5g$ ,  $\delta_d = 0.1g$  in Eq.(6); the  $g$  indicates the grinding grit size in the producing craft.  
 114 The random diffuser grit number  $G$  represents the diffuser surface roughness. We demonstrate  
 115 the Gaussian random surface-relief height in Fig.1 (c). Here, inspired by the antarctic surface  
 116 roughness model [40, 41], We model the random diffuser grit number  $G$  as the inverse of the  
 117 grinding grit size with coefficients, which could be expressed as follows:

$$g \approx \frac{1}{39.4 \times G} \times 10^6 \mu m, \quad (7)$$

118 Where the  $G$  represents the diffuser grit and the conversion ratio of inches to meters is  
 119 approximately 39.4.

## 120 2.2. Speckle correlation physical basic

121 In optical imaging systems for imaging through scattering media, the speckle correlation is an  
 122 essential method to analyze the shift-invariant properties of speckle patterns and demonstrates  
 123 its feasibility and superiority for speckle reconstruction. The scattered light field retains partial  
 124 information of the incident light field within the OME range and the speckle patterns are invariant  
 125 to little tilts or shifts for the optical imaging system. The auto-correlation of the speckle pattern  
 126 could be expressed as follows:

$$I \star I = (O * S) \star (O * S) = (O \star O) * (S \star S) = (O \star O) + C, \quad (8)$$

127 Where the  $(\star)$  represents the correlation operation and the  $(*)$  represents the convolution  
 128 operation. The auto-correlation of the optical imaging system PSF is a sharply peaked function.  
 129 Hence, the auto-correlation of the speckle pattern is approximate to the auto-correlation of the  
 130 target pattern  $(O \star O)$  from the incident light  $O$ . The constant  $C$  represents the additional  
 131 background term in speckle auto-correlation results.

132 Here, based on the proposed scattering model, the auto-correlation of the speckle pattern could  
 133 be expressed as:

$$\begin{aligned} R_I(\tau) &= ((R_O(\tau) * R_h(\tau)) \cdot R_T(\tau)) * R_h(\tau) \\ &\approx \beta R_I(\tau) + C, \end{aligned} \quad (9)$$

134 Where the  $R_I(\tau)$  and  $R_O(\tau)$  represent the auto-correlation of the incident light field  $O(x, y)$   
 135 and the scattered light field  $I(x, y)$ ;  $R_h(\tau)$  represents the auto-correlation of the angular  
 136 spectrum propagation transfer function  $h(x, y)$ ;  $R_T(\tau)$  represents the auto-correlation of the

137 complex amplitude transmittance  $T(x, y)$  of the random diffuser. Since the complex amplitude  
138 transmittance is modeled as the Gaussian distribution phase modulation, the auto-correlation  
139  $R_T(\tau)$  could be approximated to a peak function with its correlation decaying rapidly at non-zero  
140 positions. The angular spectrum propagation transfer function could be equivalent to a spatial  
141 linear filter with a wide frequency spectrum. Hence, the auto-correlation  $R_h(\tau)$  could also  
142 be approximated to a peak function. The auto-correlation of the speckle pattern could be  
143 approximated to the auto-correlation of the target pattern with  $\beta$  coefficient. The  $C$  represents the  
144 constant additional background terms in speckle auto-correlation results. To verify the feasibility  
145 of our proposed model, we utilize the 220-grit diffuser (D1) and our scattering imaging model  
146 with different grit (120, 220, and 600) parameters to calculate the auto-correlation of the speckle  
147 patterns. The results are demonstrated in Fig.1 (d), and the intensity values corresponding to the  
148 positions marked in white dotted lines are shown in Fig.1 (e). The central intensity distribution  
149 of the auto-correlation results corresponding to practical speckles and our scattering imaging  
150 model is highly consistent. Hence, based on the above physical basis, the relationship between  
151 the auto-correlation of targets and the auto-correlation of speckle patterns could provide the  
152 possibility and feasibility to replace the label information of paired speckle patterns and targets,  
153 constructing consistency constraints for imaging in different scattering conditions.

### 154 2.3. Speckle-free model design

155 In most previous DL-based methods, the model was designed to build the mapping relation from  
156 speckle patterns to target patterns. The UNet, as a typical U-type convolutional neural network,  
157 has demonstrated its feasibility and superiority in speckle reconstruction [42]. However, as a  
158 strong supervised method, the model training needs various labeled pairs of speckles and targets  
159 to optimize the network. Hence, this method's generalization capability is highly dependent  
160 on the training labeled speckle data and the method is sensitive to unseen scattering conditions.  
161 Recent physics-informed DL methods introduced physical information of the scattering imaging  
162 process to solve the model generalization problems in different scattering conditions [43, 44]. By  
163 combining the speckle correlation theory with the DL method, this method could be scalable to  
164 different scattering conditions without the need for related paired speckle data. Even though,  
165 the physics-informed methods need to collect speckle patterns to train the model and build the  
166 mapping relation between the speckle correlations and the targets. Hence, the challenges for  
167 reducing the speckle data collection still need to be addressed.

#### 168 2.3.1. Speckle-free data generation

169 Based on our scattering imaging model, we develop the speckle-free self-supervised learning  
170 method for imaging through scattering media. Unlike traditional learning-based methods, our  
171 proposed method does not need to use optical imaging systems to collect speckle data for  
172 model training and optimization. The input image of our speckle-free method is imaging  
173 targets instead of speckle patterns. The imaging targets play the roles of input images and  
174 the ground truth. Moreover, we introduce the speckle auto-correlation information into the  
175 model to provide the possibility of constructing consistency constraints for data priors in unseen  
176 scattering scenarios. The speckle-free learning method is proposed to address practical speckle  
177 reconstruction scalability challenges without collected speckle data priors.

#### 178 2.3.2. Speckle-free learning structure

179 We demonstrate the schematic diagram of the speckle-free self-supervised learning method  
180 in Fig.2. In the training process, the learning model is input with unlabeled target datasets.  
181 The imaging targets use the scattering imaging model to generate speckle patterns with several  
182 preset constant imaging parameters including light wavelength, pixel pitch, image size, and  
183 variable imaging parameters including diffuser grits and the scattering imaging distances. The

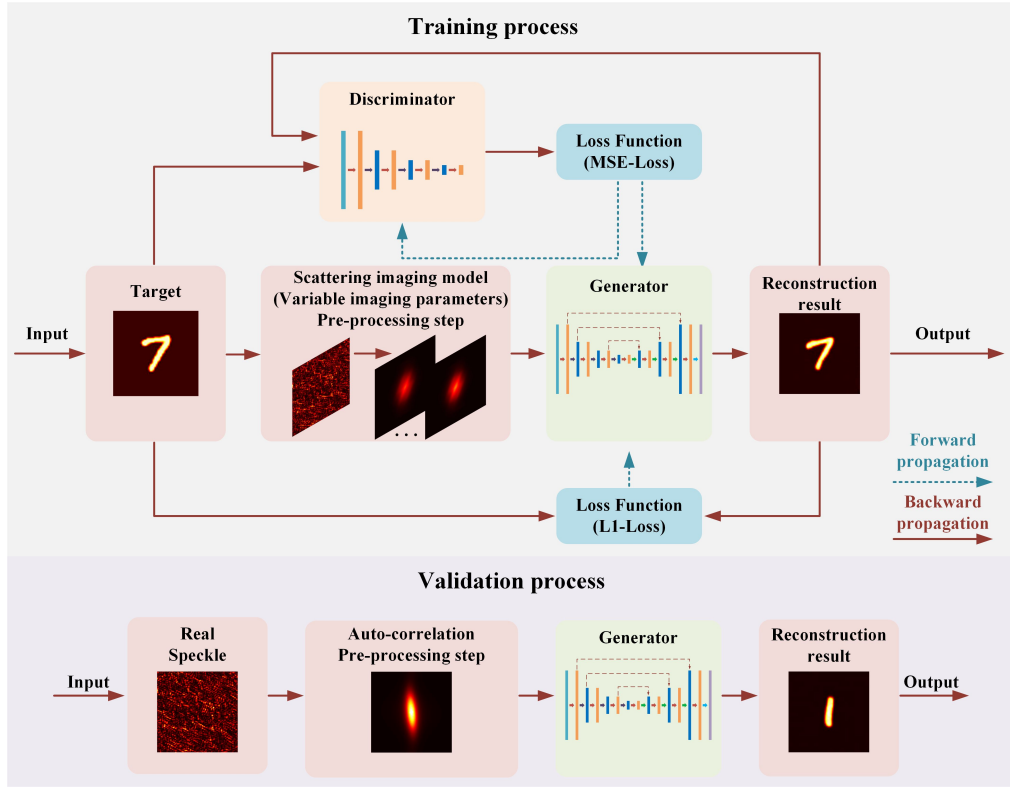


Fig. 2. Schematic diagram of the speckle-free self-supervised learning model for imaging through random diffusers. The training process utilizes the imaging target as the model's input image and ground truth. The speckle patterns using optical imaging systems are not needed for model training. The validation process utilizes the real speckle patterns as the input image for target reconstruction.

184 model extracts the relation properties of generated speckle patterns and ground truth to achieve  
185 self-supervised reconstruction.

186 In the data pre-processing step, the speckle patterns first operate the auto-correlation process  
187 to combine the physical basics with the neural network for model scalability. The speckle  
188 auto-correlation is realized through the two-dimensional Fourier inverse transform of the energy  
189 spectrum, which could be expressed as follows:

$$R(x, y) = I(x, y) \star I(x, y) = \mathcal{F}^{-1} \{ |\mathcal{F} \{ I(x, y) \}|^2 \}, \quad (10)$$

190 Where the ( $\star$ ) represents the correlation operation; the  $I(x, y)$  and  $R(x, y)$  represent the speckle  
191 patterns and auto-correlation results, and the  $\mathcal{F}$  indicates the two-dimensional Fourier transform  
192 operation.

193 In the second step of data pre-processing, we utilize several image transform operations to  
194 execute the speckle auto-correlation results. Considering the potential scattering conditions in  
195 practical optical imaging systems, we implement random adjustment of brightness and contrast,  
196 and random central magnification/demagnification to enhance the model scalability to different  
197 practical imaging scenarios such as different light intensity, background noise, signal-noise  
198 ratio (SNR), and depth-of-field(DOF) position. The speckle auto-correlation results after data  
199 augmentation are input to the neural network for training.

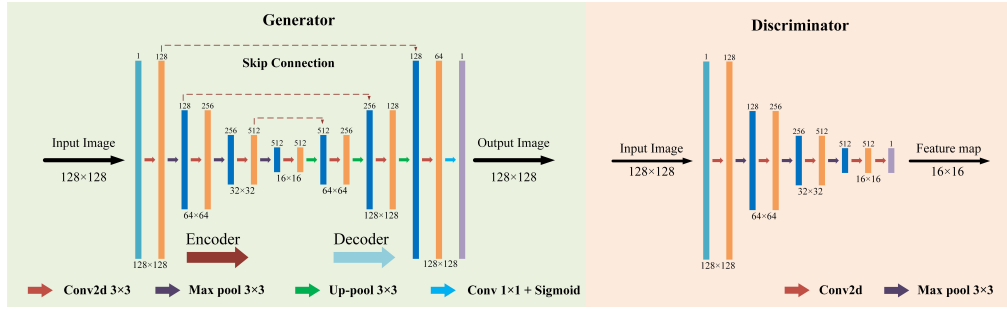


Fig. 3. The architecture of the generator and the discriminator in our proposed method.

200 In the validation process, real speckle patterns collected through practical optical imaging  
 201 systems in unseen scattering conditions are input to the model for reconstruction. The speckles  
 202 operate auto-correlations in pre-processing steps and reconstruct targets with the trained generator.

### 203 2.3.3. Speckle-free network structure

204 In the speckle-free learning method, we design a GAN network structure to learn the physical  
 205 basics and reconstruct the targets. The GAN is a learning model with a mutual game training  
 206 process, generating optimal output through adversarial generation and optimization between  
 207 two modules: the generative model and the discriminative model. The generative model is  
 208 designed to generate the image from the input speckle auto-correlation. We utilize the U-type  
 209 convolutional neural network (CNN) designed following UNet as the generator to reconstruct  
 210 targets. The discriminative model is designed to distinguish the reconstructed image and the  
 211 real target. We utilize a True/False determination CNN designed following the patchGAN as  
 212 the discriminator to capture local features of images at the fine granularity and improve the  
 213 distinguishability for details and textures. The overall architecture of the generative model and  
 214 the discriminative model is demonstrated in Fig.3. Unlike the supervised methods using speckle  
 215 as the input and target as the ground truth, the proposed method utilizes the target dataset as  
 216 both the input image and the ground truth. The consistency between the input images and the  
 217 reconstructed results is utilized as a constraint to optimize the generator in the reconstruction  
 218 process. The difference between the speckle auto-correlation result and the input target and the  
 219 consistency between the reconstructed results and the input target is utilized to optimize the  
 220 real/fake determination capability of the discriminator.

### 221 2.3.4. Speckle-free model training and optimization

222 The optimization process of the speckle-free learning method includes the optimization of the  
 223 generator and the optimization of the discriminator. The two models perform each parameter  
 224 updating process alternately as one model updates parameters while the other one remains  
 225 parameters unchanged until the two models reach a dynamic training balance. Here, we name  
 226 the target image, i.e., the input image as the Real-B; the speckle auto-correlation result as the  
 227 Real-A; and the reconstruction result as the fake. The training of the discriminator is to enhance  
 228 the model's capability to determine the truth or the false of the image. Hence, the loss function  
 229 between the Real-A and Real-B, the fake and Real-B are utilized to optimize the discriminator.  
 230 Here, we utilize the Mean Squared Error (MSE) loss as the loss function of the discriminator,  
 231 which could be expressed as follows:

$$225 \text{ MSE}(y_{\text{true}}, y_{\text{pred}}) = \frac{1}{m \times n} \sum_{i=1}^{m \times n} (y_{\text{true}_i} - y_{\text{pred}_i})^2, \quad (11)$$

232 Where the  $y_{\text{true}}$  and  $y_{\text{pred}}$  represents the  $i^{\text{th}}$  pixel value on the output of the discriminative model  
 233 and its corresponding label (0/False or 1/True); and the  $m$  and  $n$  indicates the length and width of  
 234 the image. The loss function of the discriminator combines the MSE loss of the Real-A with the  
 235 Real-B and the fake with the Real-B, which could be expressed as follows:

$$\text{Loss}_D = \frac{1}{2} (\text{MSE}(\text{Real-A}, \text{real-B}) + \text{MSE}(\text{real-A}, \text{fake})), \quad (12)$$

236 Where the  $\text{Loss}_D$  represents the loss function of the discriminator model. The MSE loss of the  
 237 determination for real or fake shares the same significance.

238 The optimization of the generator contains the similarity between the reconstruction result  
 239 and the target image and the ability to deceive the discriminator. Hence, we utilize the Mean  
 240 Absolute Error (L1-loss) as the loss function to calculate the similarity difference between the  
 241 Fake and the Real-B, which could be expressed as follows:

$$\text{L1-loss} (\hat{y}, y) = \frac{1}{m \times n} \sum_{i=1}^{m \times n} \|\hat{y}_i - y_i\|, \quad (13)$$

242 Where the  $\hat{y}$  and  $y$  indicate the  $i^{\text{th}}$  pixel value on the reconstruction result and the target; and  
 243 the  $m$  and  $n$  indicate the length and width of the image. The loss function of the generator for  
 244 optimization combines the L1-loss of Fake and Real-B with the MSE loss of Fake and Real-A,  
 245 which could be expressed as follows:

$$\text{Loss}_G = \alpha \cdot \text{MSE}(\text{Real-A}, \text{Fake}) + (1 - \alpha) \cdot \text{L1-loss}(\text{Fake}, \text{Real-B}), \quad (14)$$

246 Where the  $\text{Loss}_G$  represents the loss function of the generative model;  $\alpha$  is a hyperparameter to  
 247 adjust the weight between two loss functions, which is set as  $\alpha = 0.01$  in the proposed method.

248 In the training process of the proposed method, we utilize the adaptive moment estimation  
 249 (Adam) optimizer with  $2.5 \times 10^{-4}$  initial learning rate for the loss function minimization and  
 250 model convergence. The model validation utilizes the speckle patterns collected from the real  
 251 optical imaging system for imaging through scattering media instead of speckles generated from  
 252 the scattering imaging model. The training and validation process of the proposed method is  
 253 performed on the computer server with two graphics processing units (NVIDIA A6000) using  
 254 Pytorch with Python 3.8. The proposed method is trained with five batch-size and 1000 epochs  
 255 for up to 40 hours.

#### 256 2.4. Experiment setup

257 Here, we utilize an optical imaging system to produce speckle patterns in different scattering  
 258 conditions as the validation datasets. The schematic diagram of the optical imaging system for  
 259 speckle collection is demonstrated in Fig.4. The laser (wavelength 512 nm) passes through a set  
 260 of optical elements ( $\lambda/2$  plate, objective lens, pinhole) and expands into a collimated beam by a  
 261 lens. The target information is loaded into the beam light by an amplitude spatial light modulator  
 262 (SLM) (Holoeye Pluto, pixel pitch: 8  $\mu\text{m}$ , pixel count: 1920×1080). A group of lenses L2  
 263 ( $f=60\text{mm}$ ) and L3 ( $f=50\text{mm}$ ) composes a 4f-system to match the pixel pitches between the SLM  
 264 and camera. We utilize the ground glass diffusers with different grits (Thorlabs DG10-120-MD,  
 265 DG10-220-MD, DG10-600-MD, DG10-1500-MD) as the scattering media to produce speckle  
 266 patterns. The diffuser is connected to an operable displacement platform Miniature Hexapod  
 267 (PI-824), which supports precise displacements and rotations in three axes( $x$ ,  $y$ , and  $z$ ), as shown  
 268 in Fig.5. Finally, the speckle patterns are collected by an sCMOS camera (Hamamatsu C14440,  
 269 pixel count: 2048×2048, pixel pitch: 6.5  $\mu\text{m}$ ). The distance between the SLM plane and the  
 270 diffuser plane is 15 cm, and between the diffuser plane and the camera plane is 10 cm.

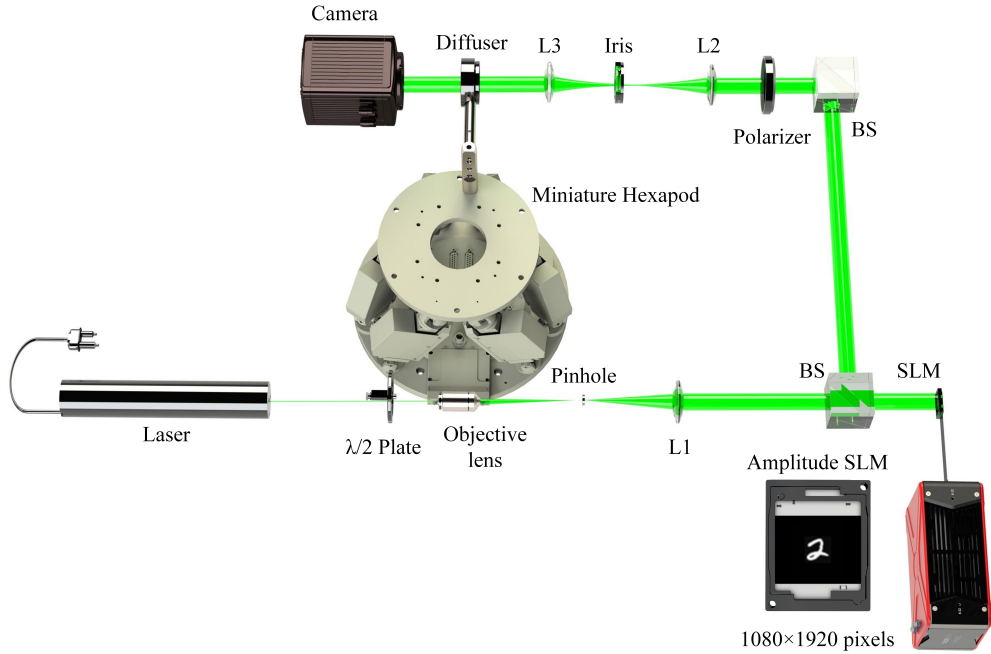


Fig. 4. Optical imaging systems for imaging through scattering media.

271    **2.5. Data acquisition**

272    Here, we explore the imaging system performance in various unknown scattering conditions  
 273    encompassing different diffusers and displacements and rotations of the diffuser plane. The targets  
 274    are selected from four datasets: MNIST handwritten digits, EMNIST handwritten letters, fashion  
 275    MNIST, and Quick-draw. The image size of the targets and speckles is set as 512×512 pixels. The  
 276    collected speckle patterns operate the auto-correlation pre-processing and then crop the central  
 277    128×128 pixels of the correlation results as the input of the model. All targets, speckle patterns,  
 278    and auto-correlation images are 8-bit gray-scale data. We utilize two comparative models, i.e., the  
 279    non-physics method and the physics-informed method using real obtained speckles to validate the  
 280    feasibility and superiority of the proposed method [45, 46]. The non-physics method reconstructs  
 281    the targets from the speckle patterns. The physics-informed method combines the physical  
 282    information of speckle patterns by adding speckle auto-correlation in pre-processing. We design  
 283    the training and validation groups for the proposed and comparative methods as follows:

284    **Training Groups:**

285    Train the speckle-free method with 10000 targets which are selected from MNIST handwritten  
 286    digits, EMNIST handwritten letters, fashion MNIST, and Quick-draw. The preset parameters  
 287    such as light wavelength, pixel pitch, and image size. The variable parameters including diffuser  
 288    grit and axial translation vary from 100 grit to 1500 grit and -20 to 20 mm. The speckles are  
 289    calculated by the scattering imaging model. The speckle correlation of data pre-processing is  
 290    realized through the Fourier transform. We apply the random resized crop, random brightness  
 291    adjustment, and random contrast adjustment to enhance the model robustness against different

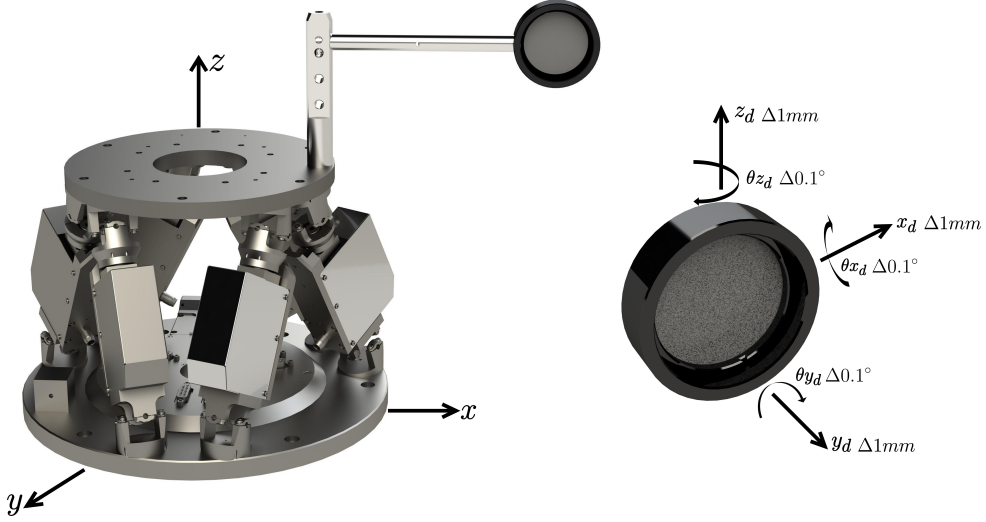


Fig. 5. The displacements and rotations of the diffuser plane. The Hexapod provides the diffuser plane with  $\pm 5\text{cm}$  ( $\Delta 1\text{mm}$ ) displacements in the x-axis and z-axis,  $\pm 15\text{cm}$  ( $\Delta 1\text{mm}$ ) displacements in the y-axis,  $\pm 0.5^\circ$  ( $\Delta 0.1^\circ$ ) rotation degrees in the x-axis, y-axis, and z-axis.

- 292 conditions in the auto-correlation data pre-processing pipeline.  
 293 Train the non-physics method with 10000 pairs of speckles and targets. The targets are selected  
 294 from MNIST handwritten digits, EMNIST handwritten letters, fashion MNIST, and Quick-draw.  
 295 The speckles are obtained through a real optical imaging system for imaging through a 220-grit  
 296 diffuser without displacements or rotations.  
 297 Train the physics-informed method with 10000 pairs of speckles and targets. The targets are  
 298 selected from MNIST handwritten digits, EMNIST handwritten letters, fashion MNIST,  
 299 and Quick-draw. The speckles are obtained through a real optical imaging system for imaging  
 300 through a 220-grit diffuser without displacements or rotations. The speckle data operates Fourier  
 301 transform-based auto-correlation pre-processing before being sent into the model for training.  
 302 **Validation Groups:**  
 303 Group 1: Validate the proposed method and comparative models with unseen scattering  
 304 conditions encompassing different diffusers and unseen targets. The validation speckles are  
 305 produced by 120, 220, 600, and 1500 grit diffusers using the optical imaging system, and the  
 306 targets are selected from unseen MNIST handwritten digits.  
 307 Group 2: Validate the proposed method and comparative models with unseen scattering  
 308 conditions encompassing different diffusers and displacements of the diffuser plane. The  
 309 validation speckles are produced by 120, 220, 600, and 1500 grit diffusers using the optical  
 310 imaging system, and the targets are selected from MNIST handwritten digits. The diffuser plane  
 311 of the optical imaging system operates -5 to 5 mm ( $\Delta 1\text{mm}$ ), -15 to 15 mm ( $\Delta 1\text{mm}$ ), and -5 to 5  
 312 mm ( $\Delta 1\text{mm}$ ) displacements in x (radial), y (axial), and z (radial) axes.  
 313 Group 3: Validate the proposed method and comparative models with unseen scattering  
 314 conditions encompassing different diffusers and rotations of the diffuser plane. The validation  
 315 speckles are produced by 120, 220, 600, and 1500 grit diffusers using the optical imaging system,  
 316 and the targets are selected from MNIST handwritten digits. The diffuser plane of the optical  
 317 imaging system operates -0.5° to 0.5° ( $\Delta 0.1^\circ$ ) rotations in x (radial), y (axial), and z (radial) axes.

318     Group 4: Validate the proposed method and comparative models with unseen scattering  
319     conditions encompassing different diffusers, different displacements, and rotations of the diffuser  
320     plane. The validation speckles are produced by 120, 220, 600, and 1500 grit diffusers using  
321     the optical imaging system, and the targets are selected from MNIST handwritten digits. The  
322     diffuser plane of the optical imaging system operates  $-0.5^\circ$  to  $0.5^\circ$  ( $\Delta 0.1^\circ$ ) rotations and -5 to 5  
323     mm ( $\Delta 1\text{mm}$ ) displacements in  $x$  (radial),  $y$  (axial), and  $z$  (radial) axes, simultaneously.

324     Group 5: Validate the proposed method and comparative models with unseen targets in  
325     other datasets. The validation speckles are produced by 220 grit diffusers using the optical  
326     imaging system and the targets are selected from Emnist handwritten letters, fashion MNIST,  
327     and Quick-draw. The scattering conditions have no displacements or rotations.

### 328     **3. Result and analysis**

#### 329     *3.1. Speckle reconstruction performance validation*

330     In this section, we compare the proposed speckle-free learning method reconstruction with  
331     two comparative methods, i.e., non-physics and physics-informed methods. The non-physics  
332     method utilized the UNet as the network structure and the physics-informed method utilized the  
333     pixel-to-pixel (P2PGAN) as its network structure. The UNet was a classical CNN end-to-end  
334     learning model with the U-type architecture and demonstrated strong speckle reconstruction  
335     capability. The P2PGAN is a state-of-the-art GAN structure with point-to-point reflection which  
336     is widely used in image style transformation, super-resolution imaging, etc. Here, we utilize the  
337     two methods as the comparative methods which utilize speckle data collected by practical optical  
338     imaging systems for model training and speckle reconstruction. The non-physics model does not  
339     contain physical information and utilizes the speckle patterns and targets as the network input and  
340     ground truth. The physics-informed combines the physical information of the speckle patterns  
341     with the model by adding the speckle auto-correlation operations in the data pre-processing step.

342     In reconstruction performance validation, we utilize unseen diffusers, unseen displacements,  
343     and unseen rotations of the diffuser plane as the scattering conditions using practical optical  
344     imaging systems to collect speckle patterns. Moreover, we utilize three scientific metrics to  
345     quantify the three methods' reconstruction performance explicitly. The Pearson Correlation  
346     Coefficient (PCC) is a normalized measure of covariance that characterizes the degree of linear  
347     correlation between two images, ranging from -1 to 1. The Structural Similarity Index (SSIM)  
348     is a metric used to assess the similarity of reconstructed images, taking into account intensity,  
349     contrast, and structural similarity. SSIM values range from 0 to 1, where 1 indicates perfect  
350     similarity and 0 indicates no similarity. The Peak Signal-to-Noise Ratio (PSNR) quantifies the  
351     quality of reconstructed images using the Mean Squared Error (MSE) on a decibel scale, with  
352     higher values indicating better image quality.

##### 353     *3.1.1. Reconstruction performance comparison with unseen diffusers.*

354     In this section, we validate the reconstruction performance of three methods for imaging through  
355     unseen diffusers. The speckle patterns for validation are produced by 120, 220, 600, and  
356     1500 grit diffusers using MNIST handwritten digits as imaging targets. The different grits of  
357     the diffusers represent the different modes of the scattering media. Hence, the reconstruction  
358     performance represents the methods' scalability to unseen diffusers. We demonstrate the  
359     reconstruction performance of three methods in Fig.6. The non-physics and physics-informed  
360     methods are trained with speckles produced by the 220-grit diffuser. The three methods  
361     demonstrate great reconstruction performance with the 220-grit diffuser while the non-physics  
362     method demonstrates degraded reconstruction performance for unseen diffusers. The average  
363     reconstruction performance for physics-informed and speckle-free methods on four diffusers  
364     achieve 0.7846, 0.8491, 20.75dB, and 0.8047, 0.8680, 20.95dB for PCC, SSIM, and PSNR

Imaging target		Reconstruction results						
Method	Training diffuser	Testing diffuser	120 grit	220 grit	600 grit	1500 grit		
Non-physics	220 grit	120 grit						
		220 grit						
		600 grit						
		1500 grit						
Physics-informed	220 grit	120 grit						
		220 grit						
		600 grit						
		1500 grit						
Speckle-free	Free parameters in scattering model	120 grit						
		220 grit						
		600 grit						
		1500 grit						

Fig. 6. Comparison of our proposed method with other methods for imaging through unseen diffusers.

metrics individually.

366    3.1.2. Reconstruction performance comparison with unseen diffusers and unseen displacements.  
 367

368    In this section, we validate the three methods of reconstruction performance in 200 scattering  
 369    conditions encompassing unseen diffusers and unseen displacements of the diffuser plane.

370    We utilize the Miniature Hexapod to control the diffuser plane which could provide precise  
 371    displacements in axes x, y, and z. The displacements of the diffuser plane in axis-x and axis-z  
 372    change the radial position of the diffuser. In other words, the x-axis and z-axis displacements  
 373    change the random diffusing surface of the scattering media. In our scattering imaging model,  
 374    the diffuser provides random complex amplitude transmittance to the incident light. Hence, the  
 375    displacements of the diffuser plane in the x or z axis represent the different distribution of the

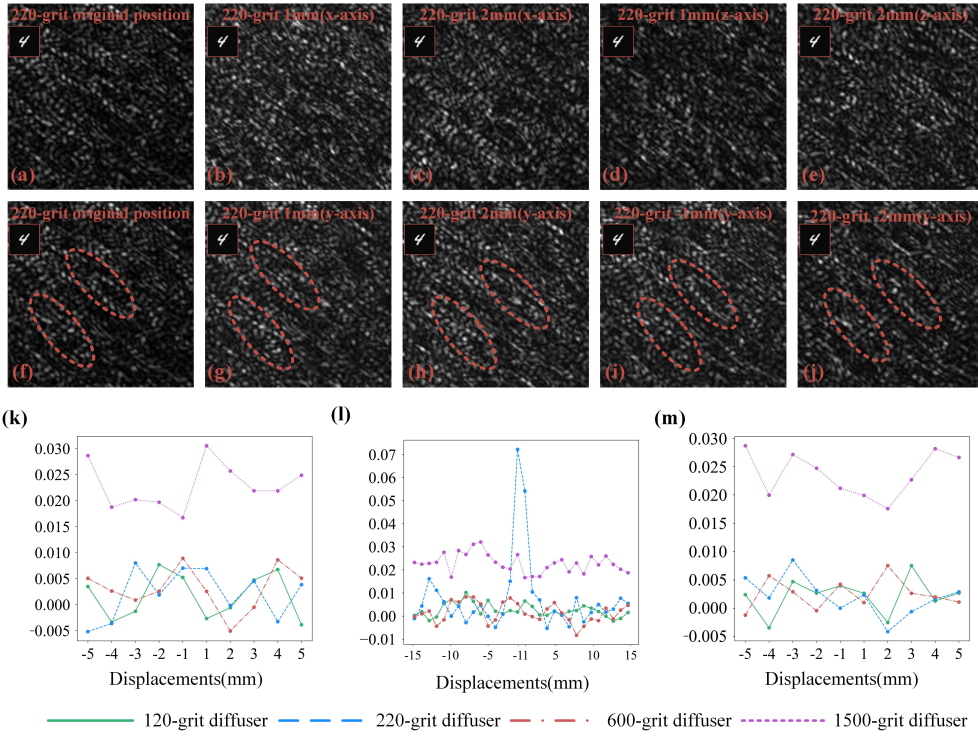


Fig. 7. (a)-(j). Speckle patterns collected with  $\pm 1/2\text{mm}$  displacements in the x-axis, z-axis, and y-axis. The similarities between speckles in the original condition and other conditions are labeled in red. (k)-(m). Cross-correlation coefficient of the speckle correlation for the optical imaging systems with different diffusers(120 grit, 600 grit, and 1500 grit) and displacements in axes x, y, and z. The displacements of axes x and z vary from -5 mm to 5 mm ( $\Delta 1\text{mm}$ ). The displacements of axis-y vary from -15 mm to 15 mm ( $\Delta 1\text{mm}$ ).

random transmittance and the speckle pattern is de-correlated to the speckle in original condition. We list speckle patterns in different scattering conditions in Fig.7 (a)-(j). The speckle patterns produced with x-axis or z-axis 1mm/2mm displacements behave irrelevant to speckles produced in the original condition, as shown in Fig.7 (b)-(e). We demonstrate the cross-correlation coefficients of the speckle patterns in different scattering conditions (different diffusers and displacements) with the original imaging condition in Fig.7 (k)-(m). We determine the original scattering imaging condition using the 220-grit diffuser with no displacement or rotation. The cross-coefficients of speckle patterns for x-axis and z-axis displacements are demonstrated in Fig.7 (k) and (m). The coefficients for all diffusers are far low and show random distribution as the displacement distances increase.

The displacements of the diffuser plane in the y-axis represent the changes in imaging distances between the diffuser plane and the detection plane. The speckle patterns produced with y-axis 1mm/2mm displacements share similarities in several parts with the original condition, as shown in Fig.7 (f)-(j) (labeled in red). The cross-coefficients of speckle patterns for y-axis displacements are demonstrated in Fig.7 (l). The cross-coefficients for the 220-grit diffuser rapidly decrease as the y-axis displacement increases. In contrast, the coefficients for other unseen diffusers are far lower and show random distribution as the displacement distances increase. Here, we determine the range of y-axis displacements from -15mm to 15mm with a 1mm interval and the range of

394 x-axis and z-axis displacement from -5mm to 5mm with a 1mm interval. Here, the forward  
 395 displacements are marked with "+" and the backward displacements are marked with "-". We  
 396 utilize the speckle patterns produced by four diffusers (120, 220, 600, and 1500 grit) with three  
 397 axes displacements as the validation data and evaluate the non-physics, physics-informed, and  
 398 speckle-free methods reconstruction performance.

399 We first validate the reconstruction performance of the three methods with unseen diffusers  
 400 and unseen displacements in the x-axis. The performance validation contains 40 scattering  
 401 conditions for four diffusers (120, 220, 600, and 1500 grit) and the displacements vary from  
 402 -5mm to 5mm ( $\Delta 1\text{mm}$ ). We demonstrate the reconstruction performance of three methods for  
 403 unseen different scattering conditions in Movie.S1. We also utilize the PCC, SSIM, and PSNR  
 404 metrics to evaluate the reconstruction performance of three methods in 40 unseen scattering  
 405 conditions, as shown in Fig.8 (a)-(c). The average reconstruction performance of our proposed  
 406 method achieves 0.779, 0.863, and 20.77dB for PCC, SSIM, and PSNR.

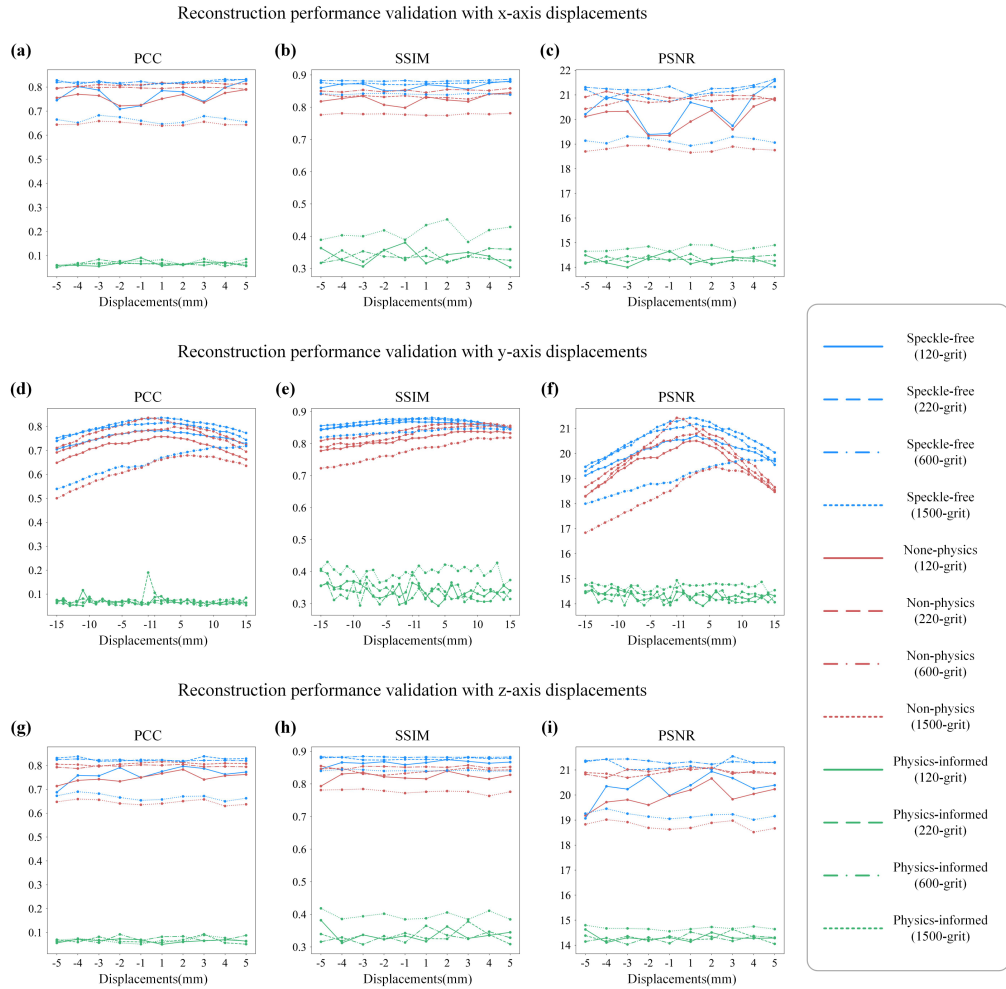


Fig. 8. The PCC, SSIM, and PSNR metrics for reconstruction performance evaluation of non-physics, physics-informed, and our speckle-free methods for imaging in 200 scattering conditions encompassing different diffuser and three-axis displacements (x,y,z).

407 Then, we validate the reconstruction performance of the three methods with unseen diffusers  
408 and unseen displacements in the y-axis. The validation contains 120 scattering conditions for  
409 four diffusers (120, 220, 600, and 1500 grit) and the displacements vary from -15mm to 15mm  
410 ( $\Delta 1mm$ ). We demonstrate the reconstruction performance of three methods for unseen different  
411 scattering conditions in Movie.S2. We also demonstrate the PCC, SSIM, and PSNR metrics for  
412 three methods' reconstruction performance in 120 unseen scattering conditions in Fig.8 (d)-(f).  
413 The average reconstruction performance of our proposed method achieves 0.773, 0.859, and  
414 20.79dB for PCC, SSIM, and PSNR.

415 We finally validate the reconstruction performance of the three methods with unseen diffusers  
416 and unseen displacements in the z-axis. The validation contains 40 scattering conditions for  
417 four diffusers (120, 220, 600, and 1500 grit) and the displacements vary from -5mm to 5mm  
418 ( $\Delta 1mm$ ). The reconstruction performance with displacements of the diffuser plane in the z-axis  
419 is similar to the x-axis. We demonstrate the reconstruction performance of three methods for  
420 unseen different scattering conditions in Movie.S3. We also demonstrate the PCC, SSIM, and  
421 PSNR metrics for three methods' reconstruction performance in 40 unseen scattering conditions  
422 in Fig.8 (g)-(i). The average reconstruction performance of our proposed method achieves 0.782,  
423 0.866, and 20.74dB for PCC, SSIM, and PSNR.

424 For imaging through unseen diffusers with unseen plane displacements in axes x, y, and z, the  
425 non-physics method demonstrates degraded reconstruction performance for unseen scattering  
426 conditions while the physics-informed and our speckle-free methods maintain consistently great  
427 reconstruction performance for unseen 200 scattering conditions. The non-physics method lacks  
428 generalization capability for unseen scattering conditions since the method is not combined with  
429 physical information of the speckle correlation properties. The free parameters in our scattering  
430 imaging model enable stronger generalization capability and better reconstruction performance  
431 than the physics-informed method since it shows larger variances for unseen scattering conditions  
432 than the original condition. According to our model, the displacements in the x and z axes  
433 change the incident diffuser surface which causes different Gaussian random distribution complex  
434 transmittance. Hence, the variable parameters in our scattering model could provide physics  
435 priors for unseen conditions speckle reconstruction. For y-axis displacements, different scattering  
436 distances could demonstrate different magnification/demagnification of the speckle correlation  
437 patterns according to Ref. [47]. Hence, we utilize multiple scattering distances as the variable  
438 imaging parameter and add random resized crop in the method pre-processing steps. As Fig.8  
439 depicts, the proposed speckle-free method demonstrates better reconstruction performance and  
440 stronger consistency than the physics-informed method although our method is not trained with  
441 practical speckle patterns.

#### 442 3.1.3. Reconstruction performance comparison with unseen diffusers and unseen rotations.

443 In this section, we validate the reconstruction performance of three methods in 120 scattering  
444 conditions encompassing unseen diffusers and unseen rotations of the diffuser plane.

445 We utilize the Miniature Hexapod to precisely rotate axes x, y, and z. We list speckle patterns  
446 collected in different scattering conditions in Fig.9 (a)-(p). The rotation of the diffuser plane in  
447 the x-axis changes the pitch degrees of the diffuser. As Fig.9 (b)-(e) shows, the speckles with little  
448 x-axis rotations share major similarities with speckles in the original position (labeled in red).  
449 We demonstrate the cross-coefficients of the speckle patterns in different scattering conditions  
450 (different diffusers and rotations) in Fig.9 (q)-(s). We determine the original scattering imaging  
451 condition using the 220-grit diffuser with no displacement or rotation. As shown in Fig.9 (q), the  
452 coefficient for the 220-grit diffuser reaches approximately 0.5 when the x-axis rotation angle is  
453  $\pm 0.1^\circ$  and decreases rapidly as the rotation degree increases.

454 The rotation of the diffuser plane in the y-axis changes the radial position of the diffuser. In  
455 other words, the y-axis rotations of the diffuser plane are similar to the little displacements in the

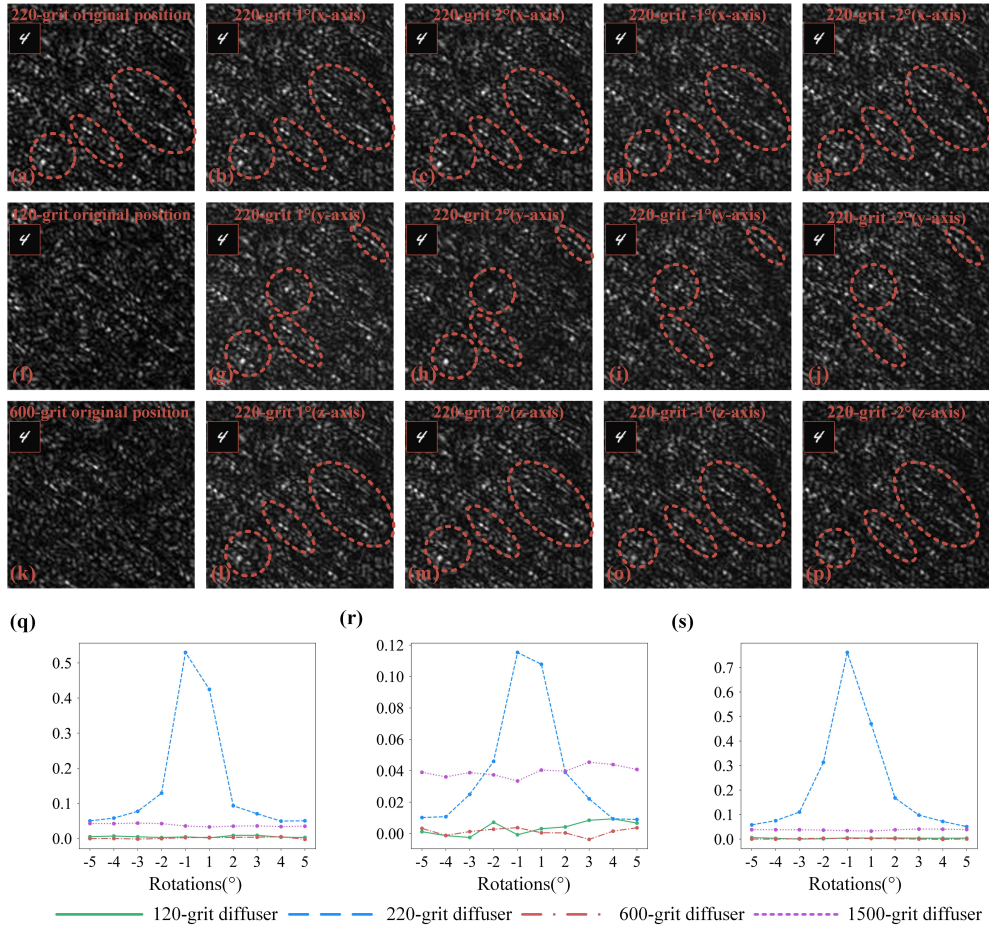


Fig. 9. (a)-(p). Speckle patterns collected with  $\pm 1/2\text{mm}$  displacements in the x-axis, z-axis, and y-axis. The similarities between speckles in the original condition and other conditions are labeled in red. (q)-(s). Cross-correlation coefficient of the speckle correlation for the optical imaging systems with different diffusers(120 grit, 600 grit, and 1500 grit) and rotations in axes x, y, and z. The rotations of axes x, y, and z vary from  $-0.5^\circ$  to  $0.5^\circ$  ( $\Delta 0.1^\circ$ ).

456 polar coordinate system. As Fig.9 (g)-(j) shows, the speckles with little y-axis rotations share  
457 several similarities with speckles in the original position (labeled in red). We demonstrate the  
458 cross-coefficients of speckles with y-axis rotations in Fig.9 (r). The coefficients for the 220-grit  
459 diffuser are lower than 0.12 and decrease rapidly as the rotation degree increases.

460 The rotation of the diffuser plane in the z-axis changes the swing degrees of the diffuser. As  
461 Fig.9 (l)-(p) shows, the speckles with little z-axis rotations share major similarities with speckles  
462 in the original position (labeled in red). We demonstrate the cross-coefficients of speckles with  
463 z-axis rotations in Fig.9 (s). The coefficients for 220-grit diffuser reach higher than 0.7 when the  
464 z-axis rotation degree is  $\pm 0.1^\circ$  and decrease rapidly as the rotation degrees increase. Moreover,  
465 changes in diffusers could lead to the decorrelation of speckle patterns. As Fig.9 (f) and (k) show,  
466 the speckles have low degrees of relevance with the original speckle. The cross-coefficients  
467 for other diffusers are lower than 0.1 and show random variation as the rotation degrees and  
468 displacement distances increase. Here, we determine the range of the x-axis, y-axis, and z-axis

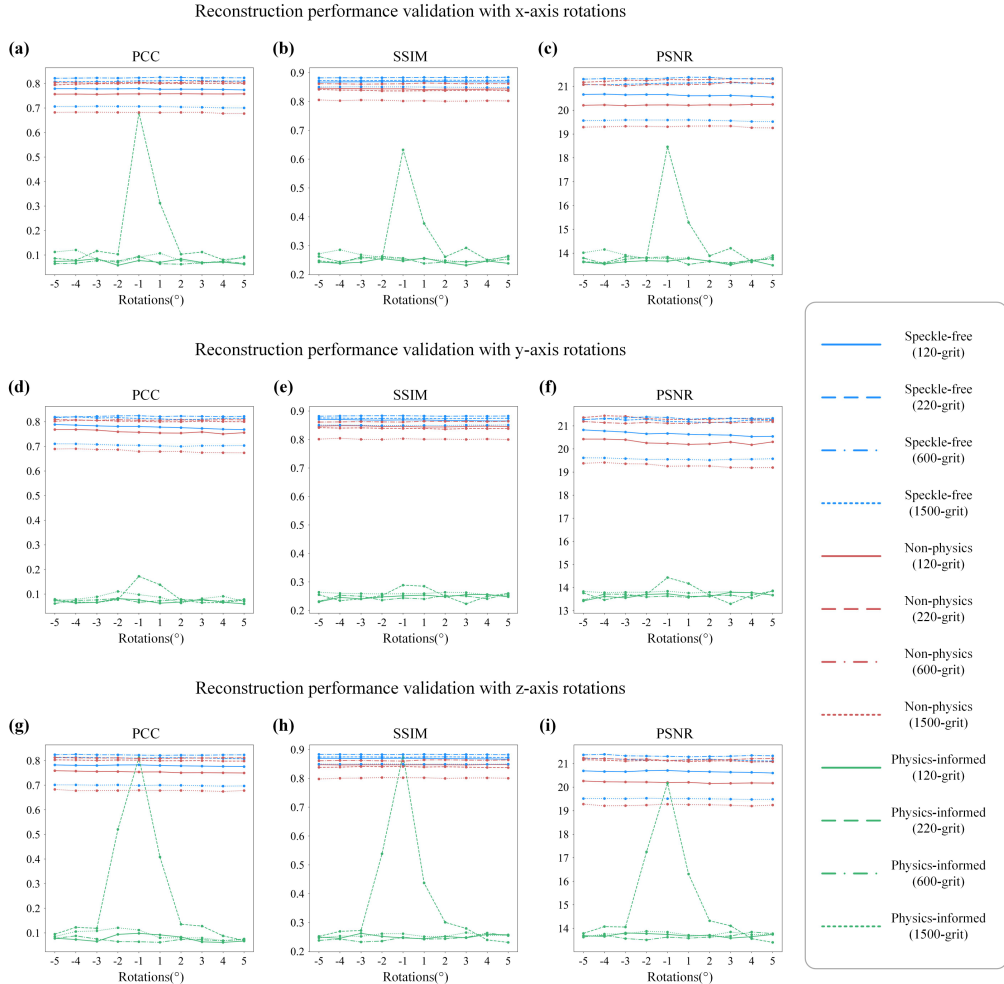


Fig. 10. The PCC, SSIM, and PSNR metrics for reconstruction performance evaluation of non-physics, physics-informed, and our speckle-free methods for imaging in 120 scattering conditions encompassing different diffuser and three-axis rotations (x,y,z).

469 rotation of the diffuser plane from  $-0.5^\circ$  to  $0.5^\circ$  with a  $\Delta 0.1^\circ$  interval. Here, the Clockwise  
 470 rotations are marked with "+" and the counterclockwise rotations are marked with "-". We utilize  
 471 the speckle patterns produced by four diffusers (120-grit, 220-grit, 600-grit, and 1500-grit) with  
 472 three axes rotations as the validation data and evaluate the non-physics, physics-informed, and  
 473 speckle-free methods reconstruction performance.

474 We first validate the reconstruction performance of the three methods with unseen diffusers  
 475 and unseen rotations in the x-axis. The performance validation contains 40 scattering conditions  
 476 for four diffusers (120, 220, 600, and 1500 grit) and the rotation degrees vary from  $-0.5^\circ$  to  $0.5^\circ$   
 477 ( $\Delta 0.1^\circ$ ). The changes in the diffuser plane's pitch degrees could influence the light transmittance  
 478 direction and change the distribution and the position of the speckle pattern. We demonstrate  
 479 the reconstruction performance of three methods for unseen different scattering conditions in  
 480 Movie.S4. We also demonstrate the PCC, SSIM, and PSNR metrics for the three methods'  
 481 reconstruction performance with unseen diffusers and unseen x-axis rotation in Fig.10 (a)-(c).  
 482 The speckle-free method achieves better reconstruction performance achieving 0.774, 0.868, and

483 20.21dB for PCC, SSIM, and PSNR, individually.

484 We then validate the reconstruction performance of the three methods with unseen diffusers  
485 and unseen rotations in the y-axis. The performance validation contains 40 scattering conditions  
486 for four diffusers (120, 220, 600, and 1500 grit) and the rotation degrees vary from  $-0.5^\circ$  to  
487  $0.5^\circ$  ( $\Delta 0.1^\circ$ ). The rotation degree changes of the diffuser plane in the y-axis could change the  
488 displacements in polar coordinate systems. In other words, the rotations of the diffuser plane  
489 will change the surface of the diffuser for the incident light. We demonstrate the reconstruction  
490 performance of three methods for unseen scattering conditions in Movie.S5. We also utilize the  
491 PCC, SSIM, and PSNR metrics to evaluate the reconstruction performance of three methods in  
492 40 unseen scattering conditions as shown in Fig.10 (d)-(f). The proposed method achieves 0.775,  
493 0.869, and 20.24dB for PCC, SSIM, and PSNR, individually.

494 We finally validate the reconstruction performance of the three methods with unseen diffusers  
495 and unseen rotations in the z-axis. The performance validation contains 40 scattering conditions  
496 for four diffusers (120, 220, 600, and 1500 grit) and the rotation degrees vary from  $-0.5^\circ$  to  
497  $0.5^\circ$  ( $\Delta 0.1^\circ$ ). The swing degrees of the diffuser plane could change the distribution and the  
498 position of the speckle pattern. We demonstrate the reconstruction performance of three methods  
499 with unseen diffusers and z-axis rotations in Movie.S6. We also demonstrate the PCC, SSIM,  
500 and PSNR metrics for the three methods' reconstruction performance with unseen diffusers  
501 and unseen z-axis rotation in Fig.10 (g)-(i). The proposed method achieves 0.773, 0.872, and  
502 20.21dB for PCC, SSIM, and PSNR, individually.

503 For imaging through unseen diffusers with unseen plane rotations in axes x, y, and z, the  
504 non-physics method demonstrates rapidly degraded reconstruction performance as the rotation  
505 degrees increase while the physics-informed and speckle-free methods demonstrate consistent  
506 great reconstruction performance for unseen scattering conditions. The non-physics method  
507 scalability for unseen scattering conditions and even little changes in speckle patterns could  
508 deteriorate the reconstruction performance. On the other hand, the introduction of physics  
509 information could enhance the physics-informed and speckle-free methods for scalable scattering  
510 conditions. The evaluation results presented in Fig.10 demonstrate that our speckle-free method  
511 has better reconstruction performance for other unseen diffusers and shows similar performance  
512 for the 220-grit diffuser compared with the physics-informed method.

#### 513 3.1.4. Reconstruction performance comparison with unseen diffusers and combinations of 514 unseen displacements and rotations.

515 In this section, we validate the three methods of reconstruction performance in 120 scattering  
516 conditions encompassing unseen diffusers and combinations of unseen displacements and  
517 rotations of the diffuser plane.

518 We utilize the Miniature Hexapod to provide precise displacement and rotations simultaneously  
519 in axes x, y, and z. We list speckle patterns collected in different scattering conditions in Fig.11  
520 (a)-(p). The combination of the diffuser plane's x-axis displacement and rotation changes the pitch  
521 degrees of the diffuser and the incident scattering surface. As Fig.11 (b)-(e) shows, the speckles  
522 with little x-axis displacements and rotations have a huge difference from speckles in the original  
523 position. We demonstrate the cross-coefficients of the speckle patterns in different scattering  
524 conditions (different diffusers, displacements, and rotations) in Fig.11 (q)-(s). We determine the  
525 original scattering imaging condition using the 220-grit diffuser with no displacement or rotation.  
526 As shown in Fig.11 (q), the coefficients for all diffusers are far low and show random variation as  
527 the x-axis rotation degrees and displacement distances increase.

528 The combination of the diffuser plane y-axis displacement and rotation changes the radial  
529 position and scattering distance of the diffuser and detection plane. As Fig.11 (g)-(j) shows, the  
530 speckles with little y-axis displacements and rotations share several similarities with speckles  
531 in the original position (labeled in red). As shown in Fig.11 (r), the coefficient for the 220-grit

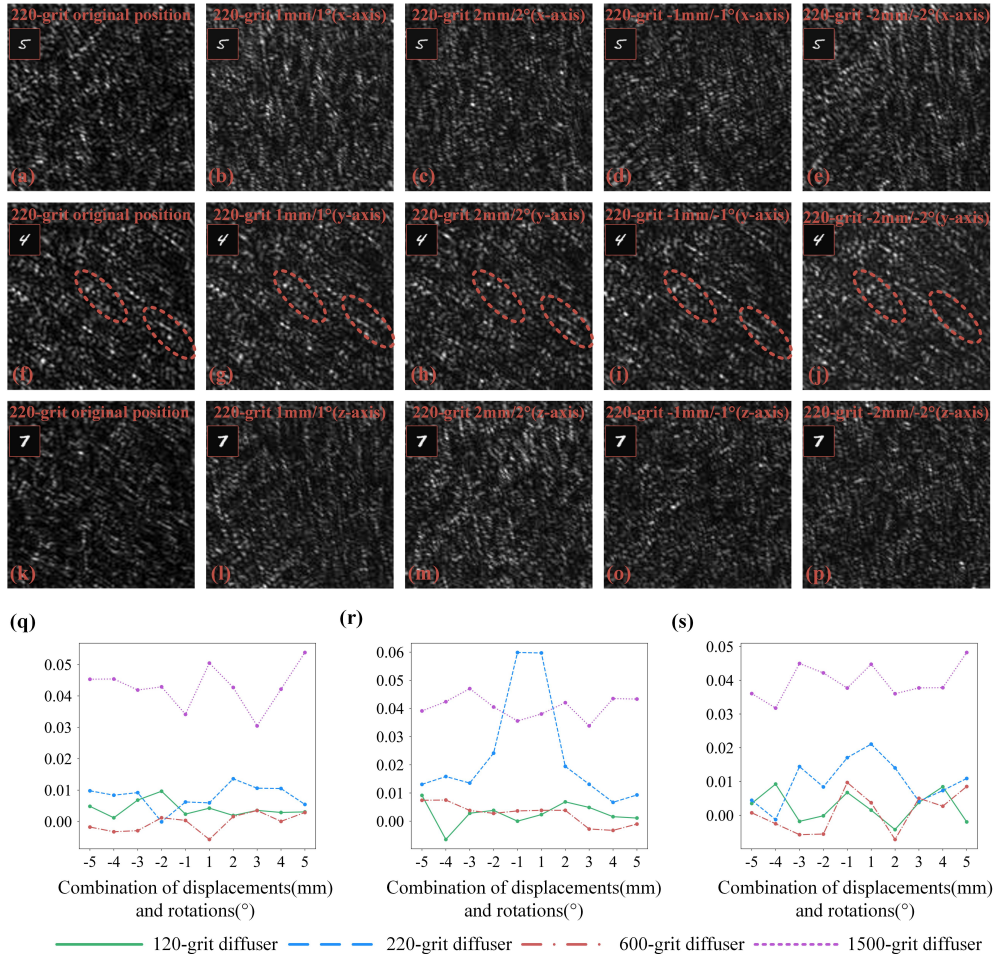


Fig. 11. (a)-(p). Speckle patterns collected with  $\pm 1/2\text{mm}$  displacements and  $\pm 1/2^\circ$  rotations in the x-axis, z-axis, and y-axis. The similarities between speckles in the original condition and other conditions are labeled in red. (q)-(s). Cross-correlation coefficient of the speckle correlation for the optical imaging systems with different diffusers(120 grit, 600 grit, and 1500 grit) and combinations of different displacements and rotations in axes x, y, and z. The combination of displacements and rotations of axes x, y, and z vary from -5mm to 5 mm ( $\Delta 1\text{mm}$ ) and  $-0.5^\circ$  to  $0.5^\circ$  ( $\Delta 0.1^\circ$ ).

532 diffuser is lower than 0.06 and decreases rapidly as the y-axis rotation degrees and displacement  
 533 distances increase while the coefficients for other diffusers show random variation as the rotation  
 534 degrees and displacement distances increase.

535 The combination of the diffuser plane z-axis displacement and rotation changes the swing  
 536 degrees and the incident scattering surface. As Fig.11 (k)-(p) shows, the speckles with little  
 537 z-axis displacements and rotations have a huge difference from speckles in the original position.  
 538 As shown in Fig.11 (s), the coefficients for all diffusers are far low and show random variation as  
 539 the z-axis rotation degrees and displacement distances increase. Here, we determine the range  
 540 of the x-axis, y-axis, and z-axis displacements and rotation combination for the diffuser plane  
 541 varying from -5mm to 5mm with a 1mm interval and  $-0.5^\circ$  to  $0.5^\circ$  with a  $\Delta 0.1^\circ$  interval. We  
 542 utilize the speckle patterns produced by four diffusers (120-grit, 220-grit, 600-grit, and 1500-grit)

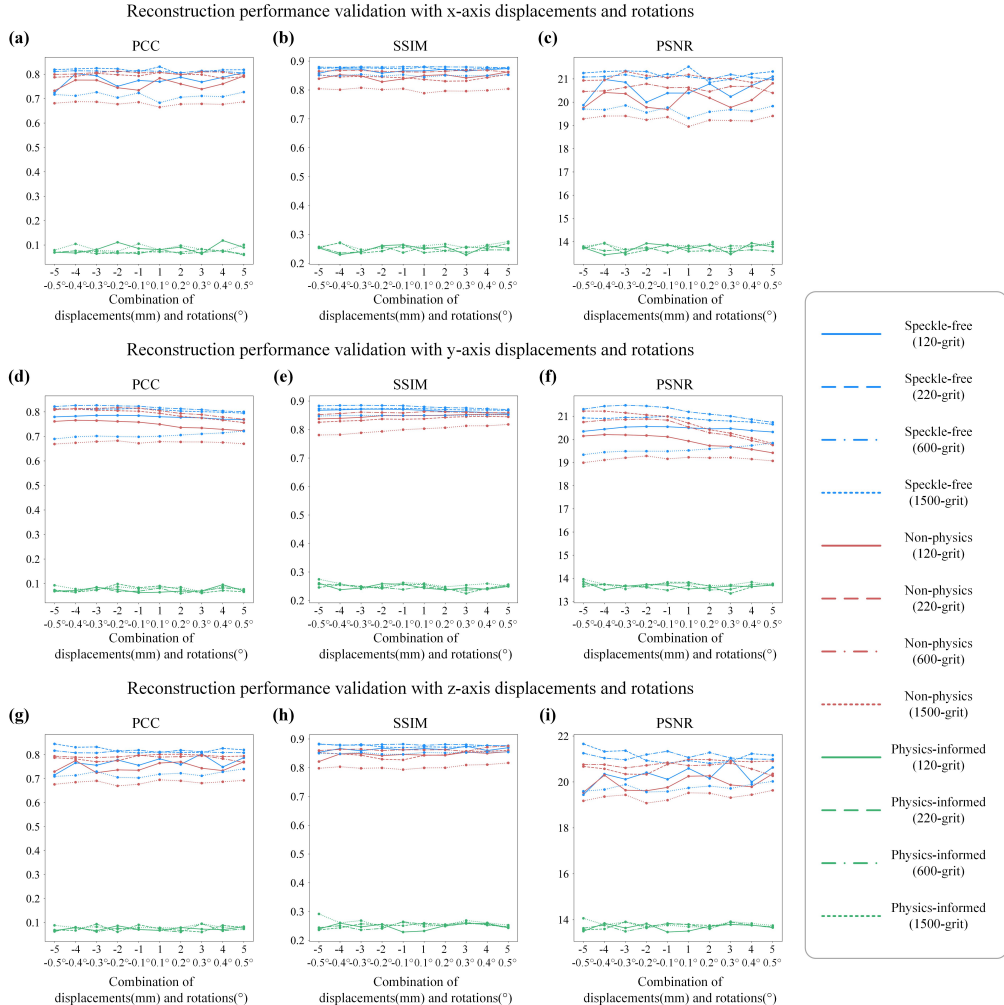


Fig. 12. The PCC, SSIM, and PSNR metrics for reconstruction performance evaluation of non-physics, physics-informed, and our speckle-free methods for imaging in 120 scattering conditions encompassing different diffuser and combinations of displacements and rotations in three axes x,y, and z.

543 with three axes displacements and rotations as the validation data and evaluate the non-physics,  
 544 physics-informed, and speckle-free methods reconstruction performance.

545 We first validate the reconstruction performance of the three methods with unseen diffusers, and  
 546 combinations of unseen displacements and rotations in the x-axis. The performance validation  
 547 contains 40 scattering conditions for four diffusers (120, 220, 600, and 1500 grit). The x-axis  
 548 displacements vary from -5mm to 5 mm ( $\Delta 1\text{mm}$ ) and the x-axis rotations vary from  $-0.5^{\circ}$  to  
 549  $0.5^{\circ}$  ( $\Delta 0.1^{\circ}$ ). We utilize the Hexapod to control the x-axis displacement and rotation of the  
 550 diffuser plane, simultaneously. We demonstrate the reconstruction performance of three methods  
 551 for unseen different scattering conditions in Movie.S7. We also demonstrate the PCC, SSIM,  
 552 and PSNR metrics for the three methods' reconstruction performance with unseen diffusers  
 553 and combinations of unseen x-axis displacements and rotations in Fig.12 (a)-(c). The average  
 554 reconstruction performance of the speckle-free method achieves 0.774, 0.868, and 20.22dB for

**Table 1. Mean values and variances of three methods' reconstruction performance for imaging in 440 scattering conditions**

		Mean value on 110 scattering positions			Variance on 110 scattering positions		
Dataset	Method	PCC	SSIM	PSNR	PCC	SSIM	PSNR
Non-physics	120-grit	0.0483	0.3359	14.2863	2.3115e-04	4.3950e-04	0.0285
	220-grit	0.0631	0.3459	14.2863	0.0105	0.0048	0.0285
	600-grit	0.0504	0.3283	14.2863	1.8815e-04	3.2988e-04	0.0285
	1500-grit	0.0523	0.4010	14.2863	1.8016e-04	4.8780e-04	0.0285
Physics-informed	120-grit	0.7762	0.8324	20.1769	0.0020	3.1811e-04	0.6390
	220-grit	0.8174	0.8491	21.1519	0.0024	3.5998e-04	1.1038
	600-grit	0.7969	0.8584	20.8035	0.0025	2.8636e-04	0.9603
	1500-grit	0.7299	0.7933	19.1028	0.0024	6.3700e-04	0.5161
Speckle-free	120-grit	0.7962	0.8601	20.7318	0.0013	1.3088e-04	0.3024
	220-grit	0.8047	0.8680	20.9527	0.0012	1.7117e-04	0.4023
	600-grit	0.7995	0.8704	21.4942	0.0011	2.2706e-04	0.4024
	1500-grit	0.7558	0.8386	20.1694	0.0021	4.9729e-05	0.4394

555 PCC, SSIM, and PSNR, individually.

556 Then, we validate the reconstruction performance of the three methods with unseen diffusers,  
 557 and combinations of unseen displacements and rotations in the y-axis. The performance validation  
 558 contains 40 scattering conditions for four diffusers (120, 220, 600, and 1500 grit). The y-axis  
 559 displacements vary from -5mm to 5 mm ( $\Delta 1\text{mm}$ ) and the y-axis rotations vary from  $-0.5^\circ$  to  
 560  $0.5^\circ$  ( $\Delta 0.1^\circ$ ). The diffuser plane operates the y-axis displacements and rotations simultaneously.  
 561 We demonstrate the reconstruction performance of three methods for unseen different scattering  
 562 conditions in Movie.S8. We also demonstrate the PCC, SSIM, and PSNR metrics for the three  
 563 methods' reconstruction performance with unseen diffusers and combinations of unseen y-axis  
 564 displacements and rotations in Fig.12 (d)-(f). The proposed method achieves better reconstruction  
 565 performance, achieving 0.771, 0.866, and 20.17dB for PCC, SSIM, and PSNR, individually.

566 We finally validate the reconstruction performance of the three methods with unseen diffusers,  
 567 and combinations of unseen displacements and rotations in the z-axis. The performance validation  
 568 contains 40 scattering conditions for four diffusers (120, 220, 600, and 1500 grit). The z-axis  
 569 displacements vary from -5mm to 5 mm ( $\Delta 1\text{mm}$ ) and the z-axis rotations vary from  $-0.5^\circ$  to  
 570  $0.5^\circ$  ( $\Delta 0.1^\circ$ ). The diffuser plane operates the z-axis displacements and rotations simultaneously.  
 571 We demonstrate the reconstruction performance of three methods for unseen different scattering  
 572 conditions in Movie.S9. We also demonstrate the PCC, SSIM, and PSNR metrics for the three  
 573 methods' reconstruction performance with unseen diffusers and combinations of unseen z-axis  
 574 displacements and rotations in Fig.12 (g)-(i). The average reconstruction performance of the  
 575 speckle-free method achieves 0.774, 0.867, and 20.21dB for PCC, SSIM, and PSNR, individually.

576 For imaging through different diffusers and combinations of displacements and rotations in

Imaging target			Reconstruction results					
Method	Training diffuser	Testing diffuser						
Non-physics	220 grit	120 grit						
		220 grit						
		600 grit						
Physics-informed	220 grit	120 grit						
		220 grit						
		600 grit						
Speckle-free	Free parameters in scattering model	120 grit						
		220 grit						
		600 grit						

Fig. 13. Comparison of our proposed method with our methods for imaging through unseen diffusers with other target datasets.

axes x, y, and z, the non-physics method demonstrates non-generalization for scalable imaging scenarios and shows degraded reconstruction performance for all unseen scattering conditions. On the other hand, the physics-informed and speckle-free methods demonstrate quite great reconstruction with plane displacements and rotations. It is worth noticing that the SSIM metric of our speckle-free method is quite stable across different diffusers, plane rotations, and displacements. In contrast, the physics-informed demonstrates higher performance for familiar diffusers than unseen diffusers. For potential scattering imaging scenarios, our speckle-free method might provide stronger generalization capability and higher reconstruction than physics-informed methods which need speckles data for training.

In Table.1, we demonstrate the mean value and variance of the three methods' reconstruction performance on 440 unseen scattering conditions encompassing 4 diffusers, 50 displacements, 30 rotations, and 30 combinations (110 scattering positions) of the diffuser plane in axes x, y, and z for PCC, SSIM, and PSNR, individually. The non-physics method demonstrates degraded reconstruction performance for all 440 unseen scattering conditions. The physics-informed and our proposed method demonstrate great reconstruction performance for unseen scattering conditions. The mean values of the physics-informed method on the 220-grit diffuser for PCC and PSNR are a little bit higher than our speckle-free methods since the model is trained with speckles produced by the 220-grit diffuser. The variance of the physics-informed method is higher than

**Table 2. Mean values and variances of three methods’ reconstruction performance for imaging with other target datasets and unseen diffusers**

		Mean value for four diffusers			Variance for four diffusers		
Dataset	Method	PCC	SSIM	PSNR	PCC	SSIM	PSNR
fashion MNIST	Non-physics	0.4203	0.5677	17.2366	0.1357	0.0463	31.6604
	Physics-informed	0.6489	0.7357	18.1693	0.0453	0.0111	19.2485
	Speckle-free	0.8151	0.8090	19.3843	0.0035	9.069e-04	1.2277
EMNIST	Non-physics	0.3525	0.4646	17.2828	0.2220	0.0827	37.4264
handwritten letters	Physics-informed	0.5608	0.7008	18.7857	0.1625	0.0375	29.9064
	Speckle-free	0.7427	0.7886	19.2485	0.0081	1.313e-05	0.5941
Quick-draw	Non-physics	0.3704	0.4965	14.6892	0.11	0.023	1.3517
	Physics-informed	0.4665	0.6850	15.3186	0.088	0.0037	2.8622
	Speckle-free	0.7014	0.8181	18.8146	0.0069	2.698e-06	0.3301

595 our speckle-free method in such conditions. Moreover, the mean values and variances for PCC,  
 596 SSIM, and PSNR of our proposed method behave better than the physics-informed method for  
 597 unseen diffusers. The evaluation results demonstrate that our proposed method is more scalable  
 598 for unseen scattering conditions and behaves more stable and robustly for generalized scattering  
 599 scenarios. Moreover, the speckle-free method does not need speckle collections and enables  
 600 the model to learn the scattering process of practical scattering imaging systems based on the  
 601 proposed scattering imaging model and several basic imaging parameters.

### 602 3.1.5. Reconstruction performance comparison on other datasets

603 In this section, we validate the reconstruction performance of three methods for imaging through  
 604 different diffusers with different targets. The speckle patterns for validation are produced by 120,  
 605 220, and 600 grit diffusers using fashion MNIST, EMNIST handwritten letters, and Quick-draw  
 606 as imaging targets [48–50]. We demonstrate the reconstruction performance of the three methods  
 607 in Fig.13. The non-physics and physics-informed methods demonstrate better reconstruction  
 608 performance with the familiar 220-grit diffuser than our speckle-free method. However, the non-  
 609 physics method demonstrates severely degraded reconstruction performance with unseen diffusers  
 610 and the physics-informed method demonstrates worse reconstruction performance than familiar  
 611 scattering conditions. Our proposed method demonstrates consistent reconstruction performance  
 612 for three unseen scattering conditions. We also demonstrate the mean values and variances  
 613 of PCC, SSIM, and PSNR metrics for three methods with three diffusers on fashion MNIST,  
 614 EMNIST handwritten letters, and Quick-draw imaging targets in Table.2. The mean values of our  
 615 method for evaluation metrics are better than the non-physics and physics-informed methods for  
 616 three imaging target datasets. The variances of the speckle-free method for evaluation metrics  
 617 are far lower than the two comparative methods, reducing by about two orders of magnitude.  
 618 The evaluation results demonstrate that the speckle-free method is more scalable for unseen  
 619 scattering conditions with more complex imaging targets. More importantly, the training costs  
 620 of our proposed method are far lower than other methods since we do not need speckle data  
 621 collection using optical imaging systems for imaging in different scattering conditions.

#### 622 4. Conclusion and discussion

623 In this study, we have proposed a scattering imaging model to characterize the physical imaging  
624 process for imaging through random diffusers and developed a speckle-free self-supervised  
625 learning method for imaging through unknown diffusers with unknown plane displacements  
626 and rotations. Unlike traditional learning-based methods for speckle reconstruction that need  
627 huge amounts of speckle data for training, our speckle-free learning method does not need to  
628 use optical imaging systems to produce speckle patterns for model training. The imaging target  
629 plays the role of the input image and ground truth in our model training. We utilize several basic  
630 imaging parameters such as light wavelength, pixel size, etc, and variable imaging parameters  
631 such as diffuser grinding grit and scattering imaging distances to generate multiple speckle  
632 patterns in the data pre-processing steps. Like the physics-informed methods, we introduce the  
633 physical information of the scattering process into our model through speckle auto-correlation  
634 operations in data pre-processing steps. Moreover, several image processing operations such  
635 as random resized crop, brightness, and contrast adjustment are used to enhance the model's  
636 robustness against different conditions.

637 We demonstrate the proposed speckle-free learning method's generalization capability and  
638 reconstruction performance through several validation groups. We collect 440 groups of speckle  
639 data in different scattering conditions using practical optical imaging systems for imaging through  
640 scattering media [51]. The 440 scattering conditions encompass four diffusers (120, 220, 600, and  
641 1500 grit), ten conditions with x-axis displacements, thirty conditions with y-axis displacements,  
642 ten conditions with z-axis displacements, thirty conditions with x/y/z axes rotations, and thirty  
643 conditions with x/y/z axes displacement and rotation combinations. The speckle-free learning  
644 method demonstrates better reconstruction performance and stronger generalization capability  
645 than physics-informed methods. More importantly, unlike physics-informed methods that have  
646 higher reconstruction performance in trained scenarios and lower performance in unseen scenarios,  
647 speckle-free methods show consistent reconstruction performance for potential scalable scattering  
648 conditions. The average reconstruction performance of the speckle-free method is higher and the  
649 variance on unseen scattering conditions is far lower than the physics-informed method. Besides,  
650 the speckle-free method overcomes the need for speckle data collection and decreases the training  
651 costs of learning models (training data) for imaging through scattering media. The speckle-free  
652 learning method could be adapted to possible imaging tasks in potential scattering scenarios to  
653 replace speckle-needed learning methods.

654 The speckle-free learning method could be further improved in several aspects in the future.  
655 On the one hand, the GAN network uses the UNet as the generator to reconstruct targets, which  
656 might pose challenges in network parameters and large amounts of computational costs. Future  
657 work may investigate lightweight network structures serving as the generator to reduce the model  
658 computational costs. On the other hand, imaging through scattering media could be roughly  
659 divided into two steps, speckle generation and inverse model construction. We believe the one  
660 important step in light scattering problems, i.e., data collection could be significantly alleviated,  
661 and the other task, i.e., the reconstruction process is possible to be realized in optical platforms.  
662 Several works have proved that the learning model based on convolution could be realized with  
663 optical techniques, such as phase modulation and optical lens systems, etc [52–55]. Hence, future  
664 work may investigate the speckle-free learning process in optical platforms. We envision that  
665 the speckle-free learning method with optical realization might fulfill the destiny of designing  
666 one-step all-optical imaging systems for imaging through scattering media.

667 In conclusion, in this work, we demonstrate a speckle-free self-supervised learning method  
668 that incorporates physical information of the scattering process for imaging through unknown  
669 diffusers in unseen scattering conditions. The proposed method realizes model training and  
670 does not need any collected speckle patterns from the optical imaging system or the label  
671 information priors of the paired data. The training costs of the proposed method are lower than

672 those of comparative methods. We validated our approach on 440 unseen scattering conditions  
673 for speckle reconstruction encompassing unseen diffusers, plane displacements, and rotations.  
674 We demonstrate that the speckle-free learning method achieves superior imaging performance,  
675 incredible consistency, and strong generalization capability for scalable scattering scenarios. Our  
676 work significantly reduces the data requirements for learning-based models, thereby paving the  
677 way for the development of one-step all-optical imaging systems capable of imaging through  
678 scattering media.

### 679 **Supplementary information**

680 The demonstration of presented three methods for speckle reconstruction in 440 scattering  
681 conditions are provided in Movies.S1-S9. Speckle data for performance validation are deposited  
682 in DOI:10.34740/kaggle/ds/5259653.

### 683 **Funding**

684 National Key R&D Program of China (Grant No.2021YFA0715400).

### 685 **Disclosures**

686 The authors declare no conflicts of interest related to this article.

### 687 **Data availability**

688 Data underlying the results presented in this paper are not publicly available but may be obtained  
689 from the authors upon reasonable request.

### 690 **References**

- 691 1. J. W. Goodman, *Speckle phenomena in optics: theory and applications* (Roberts and Company Publishers, Englewood,  
692 Colorado, 2007).
- 693 2. L. V. Wang and H.-I. Wu, *Biomedical Optics: Principles and Imaging* (Wiley-Interscience, Hoboken, New Jersey,  
694 2007).
- 695 3. G. Yao and L. V. Wang, “Theoretical and experimental studies of ultrasound-modulated optical tomography in  
696 biological tissue,” *Appl. Opt.* **39**, 659–664 (2000).
- 697 4. G. Satat, M. Tancik, and R. Raskar, “Towards photography through realistic fog,” in *2018 IEEE International  
698 Conference on Computational Photography (ICCP)*, (IEEE, 2018), pp. 1–10.
- 699 5. A. P. Mosk, A. Lagendijk, G. Lerosey, and M. Fink, “Controlling waves in space and time for imaging and focusing  
700 in complex media,” *Nat. Photonics* **6**, 283–292 (2012).
- 701 6. K. Wang *et al.*, “Direct wavefront sensing for high-resolution *in vivo* imaging in scattering tissue,” *Nat. Commun.* **6**,  
7276 (2015).
- 703 7. S. Popoff, G. Lerosey, M. Fink, *et al.*, “Image transmission through an opaque material,” *Nat. Commun.* **1**, 81 (2010).
- 704 8. A. Boniface, J. Dong, and S. Gigan, “Non-invasive focusing and imaging in scattering media with a fluorescence-based  
705 transmission matrix,” *Nat. Commun.* **11**, 6154 (2020).
- 706 9. E. Tajahuerce *et al.*, “Image transmission through dynamic scattering media by single-pixel photodetection,” *Opt.  
707 Express* **22**, 16945–16955 (2014).
- 708 10. Y.-K. Xu *et al.*, “Is ghost imaging intrinsically more powerful against scattering?” *Opt. Express* **23**, 32993–33000  
709 (2015).
- 710 11. S. K. Sahoo, D. Tang, and C. Dang, “Single-shot multispectral imaging with a monochromatic camera,” *Optica* **4**,  
1209–1213 (2017).
- 712 12. X. Xu *et al.*, “Imaging objects through scattering layers and around corners by retrieval of the scattered point spread  
713 function,” *Opt. Express* **25**, 32829–32840 (2017).
- 714 13. J. Bertolotti *et al.*, “Non-invasive imaging through opaque scattering layers,” *Nature* **491**, 232–234 (2012).
- 715 14. O. Katz, P. Heidmann, M. Fink, and S. Gigan, “Non-invasive single-shot imaging through scattering layers and  
716 around corners via speckle correlations,” *Nat. Photonics* **8**, 784–790 (2014).
- 717 15. Y. LeCun, Y. Bengio, and G. Hinton, “Deep learning,” *nature* **521**, 436–444 (2015).
- 718 16. G. Barbastathis, A. Ozcan, and G. Situ, “On the use of deep learning for computational imaging,” *Optica* **6**, 921–943  
719 (2019).
- 720 17. E. Moen *et al.*, “Deep learning for cellular image analysis,” *Nat. Methods* **16**, 1233–1246 (2019).

- 721 18. H. Chen, Y. Gao, X. Liu, and Z. Zhou, "Imaging through scattering media using speckle pattern classification based  
722 support vector regression," *Opt. Express* **26**, 26663–26678 (2018).
- 723 19. S. Gigan *et al.*, "Roadmap on wavefront shaping and deep imaging in complex media," *J. Phys. Photonics* **4**, 042501  
724 (2022).
- 725 20. X. Xie *et al.*, "Extended depth-resolved imaging through a thin scattering medium with psf manipulation," *Sci. Rep.* **8**, 4585 (2018).
- 726 21. M. Liao *et al.*, "Extending the depth-of-field of imaging systems with a scattering diffuser," *Sci. Rep.* **9**, 7165 (2019).
- 727 22. D. J. Brady, L. Fang, and Z. Ma, "Deep learning for camera data acquisition, control, and image estimation," *Adv.  
728 Opt. Photonics* **12**, 787–846 (2020).
- 729 23. N. Wijethilake *et al.*, "Deep-squared: deep learning powered de-scattering with excitation patterning," *Light. Sci. &  
730 Appl.* **12**, 228 (2023).
- 731 24. Y. Wang, H. Wang, and M. Gu, "High performance "non-local" generic face reconstruction model using the  
732 lightweight speckle-transformer (spt) unet," *Opto-Electron. Adv.* **6**, 220049–1 (2023).
- 733 25. Y. Shi *et al.*, "Imaging consecutive targets through scattering medium and around corners beyond the optical memory  
734 effect using untrained network," *Results Phys.* **51**, 106691 (2023).
- 735 26. Z. Huang, Z. Gu, M. Shi, *et al.*, "An s-cnn-based phase conjugation method in imaging through random media," *Opt.  
736 Laser Eng.* **175**, 108019 (2024).
- 737 27. Y. Liu, G. Hu, X. Chu, *et al.*, "Deep learning based coherent diffraction imaging of dynamic scattering media," *Opt.  
738 Express* **31**, 44410–44423 (2023).
- 739 28. S. Li, M. Deng, J. Lee, *et al.*, "Imaging through glass diffusers using densely connected convolutional networks,"  
740 *Optica* **5**, 803–813 (2018).
- 741 29. Y. Li, Y. Xue, and L. Tian, "Deep speckle correlation: a deep learning approach toward scalable imaging through  
742 scattering media," *Optica* **5**, 1181–1190 (2018).
- 743 30. Y. Sun, J. Shi, L. Sun, *et al.*, "Image reconstruction through dynamic scattering media based on deep learning," *Opt.  
744 Express* **27**, 16032–16046 (2019).
- 745 31. Y. Wang *et al.*, "High-generalization deep sparse pattern reconstruction: feature extraction of speckles using  
746 self-attention armed convolutional neural networks," *Opt. Express* **29**, 35702–35711 (2021).
- 747 32. Z. Li *et al.*, "Self-supervised dynamic learning for long-term high-fidelity image transmission through unstabilized  
748 diffusive media," *Nat. Commun.* **15**, 1498 (2024).
- 749 33. S. Zhu, E. Guo, J. Gu, *et al.*, "Imaging through unknown scattering media based on physics-informed learning,"  
750 *Photon. Res.* **9**, B210–B219 (2021).
- 751 34. X. Hu *et al.*, "Adaptive inverse mapping: a model-free semi-supervised learning approach towards robust imaging  
752 through dynamic scattering media," *Opt. Express* **31**, 14343–14357 (2023).
- 753 35. Y. Shi, E. Guo, L. Bai, and J. Han, "Prior-free imaging unknown target through unknown scattering medium," *Opt.  
754 Express* **30**, 17635–17651 (2022).
- 755 36. S. Feng, C. Kane, P. A. Lee, and A. D. Stone, "Correlations and fluctuations of coherent wave transmission through  
756 disordered media," *Phys. review letters* **61**, 834 (1988).
- 757 37. I. Freund, M. Rosenbluh, and S. Feng, "Memory effects in propagation of optical waves through disordered media,"  
758 *Phys. review letters* **61**, 2328 (1988).
- 759 38. O. Katz, P. Heidmann, M. Fink, and S. Gigan, "Non-invasive single-shot imaging through scattering layers and  
760 around corners via speckle correlations," *Nat. Photonics* **8**, 784–790 (2014).
- 761 39. M. Kowalczyk, "Spectral and imaging properties of uniform diffusers," *JOSA A* **1**, 192–200 (1984).
- 762 40. M. Griswold, M. Harrison, and D. Saltzberg, "Observation of light transmission through randomly rough glass  
763 surfaces beyond the critical angle," *JOSA A* **24**, 3207–3210 (2007).
- 764 41. B. Daub *et al.*, "Optical modeling of the effect of surface roughness on detection of signals from within the ice with  
765 anita," (2006).
- 766 42. O. Ronneberger, P. Fischer, and T. Brox, "U-net: Convolutional networks for biomedical image segmentation," in  
767 *Medical image computing and computer-assisted intervention—MICCAI 2015: 18th international conference, Munich,  
768 Germany, October 5–9, 2015, proceedings, part III* 18, (Springer, 2015), pp. 234–241.
- 769 43. Y. Li, S. Cheng, Y. Xue, and L. Tian, "Displacement-agnostic coherent imaging through scatter with an interpretable  
770 deep neural network," *Opt. Express* **29**, 2244–2257 (2021).
- 771 44. S. Zhu *et al.*, "Efficient color imaging through unknown opaque scattering layers via physics-aware learning," *Opt.  
772 Express* **29**, 40024–40037 (2021).
- 773 45. Z. Zhou, M. M. Rahman Siddiquee, N. Tajbakhsh, and J. Liang, "Unet++: A nested u-net architecture for medical  
774 image segmentation," in *Deep Learning in Medical Image Analysis and Multimodal Learning for Clinical Decision  
775 Support: 4th International Workshop, DLMIA 2018, and 8th International Workshop, ML-CDS 2018, Held in  
776 Conjunction with MICCAI 2018, Granada, Spain, September 20, 2018, Proceedings* 4, (Springer, 2018), pp. 3–11.
- 777 46. P. Isola, J.-Y. Zhu, T. Zhou, and A. A. Efros, "Image-to-image translation with conditional adversarial networks," in  
778 *Proceedings of the IEEE conference on computer vision and pattern recognition*, (2017), pp. 1125–1134.
- 779 47. S. Zhu *et al.*, "Displacement-sensible imaging through unknown scattering media via physics-aware learning," *Opt.  
780 Laser Eng.* **160**, 107292 (2023).
- 781 48. G. Cohen, S. Afshar, J. Tapson, and A. Van Schaik, "Emnist: Extending mnist to handwritten letters," in *2017  
782 international joint conference on neural networks (IJCNN)*, (IEEE, 2017), pp. 2921–2926.

- 784 49. H. Xiao, K. Rasul, and R. Vollgraf, “Fashion-mnist: a novel image dataset for benchmarking machine learning  
785 algorithms,” arXiv preprint arXiv:1708.07747 (2017).
- 786 50. D. Ha and D. Eck, “A neural representation of sketch drawings,” arXiv preprint arXiv:1704.03477 (2017).
- 787 51. Z. Huang, “Speckle data,” (2024).
- 788 52. Y. Li and L. Tian, “Computer-free computational imaging: optical computing for seeing through random media,”  
789 Light. Sci. & Appl. **11**, 37 (2022).
- 790 53. Z. Cai *et al.*, “Lensless light-field imaging through diffuser encoding,” Light. Sci. & Appl. **9**, 143 (2020).
- 791 54. Z. Huang, Z. Gu, M. Shi, *et al.*, “Op-fcnn: an optronic fully convolutional neural network for imaging through  
792 scattering media,” Opt. Express **32**, 444–456 (2024).
- 793 55. Y. Zhang *et al.*, “Memory-less scattering imaging with ultrafast convolutional optical neural networks,” Sci. Adv. **10**,  
794 eadn2205 (2024).